Journal of Materials Chemistry A

ROYAL SOCIETY OF CHEMISTRY

PAPER

View Article Online
View Journal | View Issue

Cite this: J. Mater. Chem. A, 2021, 9, 13220

Polyacetylene derivatives in perovskite solar cells: from defect passivation to moisture endurance†

Jiexuan Jiang,‡[a] Xianhua Lang,‡[a] Qiugui Zeng,[a] M. Bilal Faheem,[a] Shanshan Rong,[a] Hui Zhao[b] and Yanbo Li*[ac]

Received 28th December 2020
Accepted 30th April 2021

DOI: 10.1039/d0ta12509a

rsc.li/materials-a

The last decade has witnessed the exploration of exceptional optoelectronic and photovoltaic properties of perovskite solar cells (PSCs) at the laboratory scale. Unfortunately, their sensitivity to moisture causes bulk degradation, hindering the commercialization of PSC devices. Despite the numerous strategies that have been developed to date in this field, effective passivation against moisture remains highly challenging. Here, we report a novel approach based on the incorporation of polyacetylene derivatives into the perovskite active layer to yield perovskite films with larger grains, lower defect density, and excellent robustness with respect to moisture. Moreover, it is revealed that the reduced trap-state density of these films is most likely due to the efficient coordination between the carboxylate moieties in the polymer and the undercoordinated Pb^{2+} in the perovskite. Upon adopting the polymer-doped perovskite as an active layer in inverted planar heterojunction PSCs with all-inorganic charge extraction layers, the power conversion efficiency (PCE) is improved to 20.41%, which is the highest value reported to date for this type of PSC to the best of our knowledge. Most importantly, the optimized device retained 90% of its initial PCE after aging in ambient air for 60 days due to its dual mechanism of moisture resistance. This work highlights an approach for developing high-performance PSCs with improved moisture stability and paves the way for their potential commercialization.

Introduction

In recent years, organic–inorganic hybrid perovskites have attracted extensive attention due to their exceptional optoelectronic properties such as high absorption coefficients, long carrier diffusion lengths, suitable band gap and energy levels, and their facile and low-cost synthesis processes.[1–5] Hybrid perovskites are widely utilized in a variety of optoelectronic devices such as photodetectors, light-emitting diodes, and solar cells.[6,7] The efficiency of perovskite solar cells (PSCs) has been increased remarkably from 3.8% to 25.5% in only a decade,[8–12] making them promising competitors to silicon-based photovoltaics and some of the most competitive next-generation energy-harvesting material candidates.[13–16]

A PSC device consists of a perovskite active layer, selective charge (electron and hole) transporting layers (CTLs), and carrier collection layers (front-electrode or substrate and metallic counter-electrode). Each layer plays an important role in the overall device performance.[17–22] Among the different proposed device architectures, PSCs with all-inorganic selective CTLs show a unique advantage in improving the device stability by replacing the commonly used but relatively unstable organic charge-transporting materials.[23] This type of device was first demonstrated by Yang *et al.* who used a NiO_x hole transporting layer (HTL) and a ZnO electron transporting layer (ETL) and demonstrated a maximum power conversion efficiency (PCE) of 16.1%.[24] We recently achieved a maximum PCE of over 19% using electron-beam-deposited NiO_x and Nb_2O_5 as the HTL and ETL, respectively.[25,26] However, in this type of device, the overall device efficiency and stability are still significantly affected by the perovskite active layer. Due to the existence of undercoordinated ions on the surface and at the grain boundaries of the perovskite active layer,[27–32] further improvement in device efficiency and stability is still necessary. Meanwhile, a high surface defect density within the perovskite layer may also contribute to a large current density–voltage (J–V) hysteresis.[33–36] It was shown that by increasing the perovskite grain size and using passivation techniques, the solar cell performance can be considerably enhanced.[37–40] It has been found that perovskite thin films with improved morphology and better crystallinity can be achieved by incorporating appropriate polymers into the perovskite precursor solution.[41–43] In particular, polymers containing weak acids, amino groups, and ionic groups with electron lone pairs were found to be effective in passivating the trap

[a]Institute of Fundamental and Frontier Sciences, University of Electronic Science and Technology of China, Chengdu 610054, China. E-mail: yanboli@uestc.edu.cn

[b]School of Chemical Engineering, Sichuan University, Chengdu 610065, China

[c]Engineering Research Center of Advanced Functional Material Manufacturing of Ministry of Education, Zhengzhou University, Zhengzhou 450001, China

† Electronic supplementary information (ESI) available. See DOI: 10.1039/d0ta12509a

‡ These authors contributed equally to this work.

states within perovskites, enabling enhanced carrier transport and collection.[44–47] Through the incorporation of semiconductor polymer dopants with good electrical conductivity, Liu *et al.*[48] and Han *et al.*[49,50] realized greatly improved device performance for PSCs. On the other hand, Zhao *et al.* reported that only chemically inert polymers can be utilized to achieve effective carrier transport.[51] Very recently, Li *et al.*[52] discovered that doping of a graphdiyne derivative into the perovskite layer can increase the size of the crystalline grains. Motivated by these results, we propose to further improve the efficiency and stability of the all-inorganic CTL-based PSCs by doping the perovskite with polyacetylene-based polymers. To date, these polymers have not been used for perovskite doping and this strategy has not been applied to all-inorganic CTL-based PSCs.

In this work, small amounts of highly conductive polyacetylene derivatives are added to the perovskite precursor solution, leading to a significant improvement in the overall device performance. The polyacetylene derivatives affect the crystallization of the perovskite layer to yield high-quality, uniform films with larger grain sizes. In addition, it is found that the polyacetylene derivative additives not only improve the carrier dynamics and passivate the perovskite surface defects, but also enhance the PSC device stability. Upon adopting the perovskite doped with a polyacetylene derivative as the active layer in inverted planar heterojunction PSCs with all-inorganic CTLs, a champion PCE of 20.41% is achieved, together with a significantly improved device stability against moisture ingress. The improved efficiency and stability of the PSC is attributed to the increased grain size, decreased trap-state density, more favorable band alignment for charge extraction, and good hydrophobicity of the polyacetylene-derivative-doped perovskite active layer.

Results and discussion

Polyacetylene-derivative polymers were used to improve the chemistry of the perovskite precursor solution and to control the nucleation and crystallization of the deposited perovskite thin films. Moreover, we fabricated inverted planar heterojunction PSCs with the ITO/NiO_x/$FA_{0.85}MA_{0.15}PbI_{2.55}Br_{0.45}$/$Nb_2O_5$/Ag device structure, as shown in Fig. 1a. A representative cross-sectional scanning electron microscopy (SEM) image of the device structure is presented in Fig. 1b. Four polymer semiconductor materials, namely polyacetylene, pentafluorophenyl (PFP) ester-functionalized poly(phenylacetylene)s, poly(4′-trifluoromethylphenyl acetylene), and triphenylamine (TPA)-functionalized polyacetylenes (denoted as P1, P2, P3, and P4, respectively) were used as additives to dope the perovskite active layer. Fig. 1c shows the molecular structures of polyacetylene and its derivatives. The successful synthesis of the polyacetylene derivatives was confirmed by nuclear magnetic resonance (NMR) spectroscopy (Fig. S1–S6†). All of the polymers can be well-dissolved in *N*,*N*-dimethylformamide (DMF), forming clear solutions without precipitates (Fig. S7†). The device performance characteristics for different polymer-doped PSCs were compared to identify the best polymer dopant. Fig. 1d presents the *J*–*V* curves for the reference PSC device and for the PSCs with different polymer additives. The photovoltaic parameters of the PSC devices are summarized in Table 1. All of the devices with the polymer-doped perovskite absorber show significantly increased short-circuit current density (J_{SC}) and fill factor (FF), particularly for the P2-doped PSC that showed a champion performance.

To further optimize the PSC device, the concentration of the P2 dopant was varied between 0.2 and 0.6 mM. Fig. 1e shows the

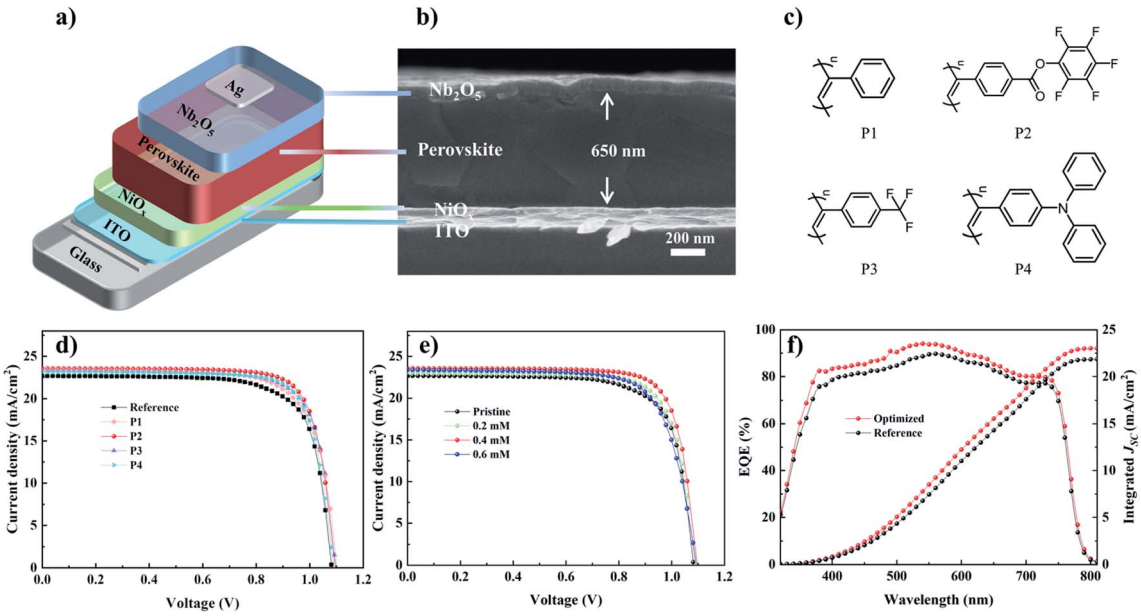

Fig. 1 (a) Schematic of the perovskite solar cell. (b) Cross-sectional SEM image of the PSC device. (c) Molecular structures of the polyacetylene-derivative polymers used in this study. (d) *J*–*V* characteristics of the PSCs doped with different polymers. (e) *J*–*V* characteristics of the PSCs doped with different P2 concentrations. (f) EQE spectra and integrated J_{SC} with and without P2.

Table 1 The key *J–V* parameters of the PSCs doped with different polymers

Polymer (0.4 mM)	V_{OC} (V)	J_{SC} (mA cm^{-2})	FF (%)	PCE (%)
Reference	1.083	22.66	74.5	18.28
P1	1.104	23.38	74.1	19.13
P2	1.098	23.59	78.8	20.41
P3	1.099	23.32	75.8	19.42
P4	1.094	23.11	78.1	19.74

J–V curves for the PSCs fabricated with different P2 concentrations, with the key photovoltaic parameters summarized in Table 2. The pristine PSC device (without P2) delivered a PCE of 18.28%, with an open-circuit voltage (V_{OC}) of 1.083 V, J_{SC} of 22.66 mA cm^{-2}, and FF of 74.5%. With the incorporation of a small amount of P2 (0.2 mM), the performance of the PSC was significantly improved. The PCE was raised to 19.13%, with the corresponding V_{OC}, J_{SC}, and FF of 1.091 V, 23.06 mA cm^{-2}, and 76.0%, respectively. It is clear that the P2-modified perovskite absorber dramatically enhances the device performance. When the P2 concentration was further increased to 0.4 mM, an impressive rise in the PCE (20.41%) was observed, with enhanced V_{OC}, J_{SC}, and FF of 1.098 V, 23.59 mA cm^{-2}, and 78.8%, respectively. It is important to note that both J_{SC} and FF were increased substantially through the optimization of the P2 content by increasing its concentration. This noticeable rise in photovoltaic parameters is attributed to the good crystallinity of the perovskite grains, suppressed Shockley–Read–Hall recombination, and smooth carrier transport from the perovskite bulk that were achieved by P2 doping, as will be discussed later. When the P2 concentration was further increased to 0.6 mM, the device performance showed a decline in the PCE to 18.67% with V_{OC}, J_{SC}, and FF of 1.093 V, 23.37 mA cm^{-2}, and 73.1%, respectively, showing that the perovskite properties are optimal at a P2 additive concentration of 0.4 mM. Fig. 1f presents the external quantum efficiency (EQE) spectra for the optimized and reference PSCs which also confirm the *J–V* scans taken under simulated sunlight. Compared to the pristine device, the EQE of the optimized devices was enhanced dramatically with the integrated J_{SC} improved to 23.03 mA cm^{-2}, which was significantly higher than the integrated J_{SC} of 21.86 mA cm^{-2} obtained for the pristine device.

To further investigate the origin of the improved PSC performance, the morphology of the perovskite films was characterized. Fig. 2a–d show the top-view SEM images of the different P2 concentration modified perovskite films. Low-magnification SEM images in Fig. S8† show that the P2-modified perovskite films have fewer pin-holes than the pristine film. The corresponding grain size distributions are statistically summarized by histograms in Fig. 2e–h. The average grain size of the four perovskite films was found to be 240, 291, 349, and 279 nm, for the pristine film and the films with 0.2 mM, 0.4 mM and 0.6 mM P2, respectively. This illustrates the beneficial effect of P2 incorporation on the nucleation and growth of perovskite crystalline grains. Moreover, it was also observed that a small number of platelets with bright contrast were distributed on the surface of the P2-doped films. According to previous reports,[53–56] the bright platelets are most likely PbI_2 that can passivate the grain boundaries and surface of perovskite films to improve the device performance.

Table 2 The key *J–V* parameters of the PSCs with different P2 concentrations

Polymer P2 (mM)	V_{OC} (V)	J_{SC} (mA cm^{-2})	FF (%)	PCE (%)
0	1.083	22.66	74.5	18.28
0.2	1.091	23.06	76.0	19.13
0.4	1.098	23.59	78.8	20.41
0.6	1.093	23.37	73.1	18.67

To study the structural and optical properties of the perovskite films, four representative samples with different P2 concentrations (0, 0.2, 0.4, and 0.6 mM) were prepared and characterized. Fig. 2i presents the X-ray diffraction (XRD) patterns showing that the incorporation of P2 made a key contribution to the improved crystallization of perovskite films and the peak of the PbI_2 phase was also slightly enhanced, which is consistent with the SEM observations. This may be ascribed to the interaction between P2 and the FA^+ and MA^+ cations that caused a small amount of PbI_2 to escape from the perovskite surface. Fig. 2j shows the UV-vis absorption spectra for the pristine perovskite films and the films with different P2 concentrations deposited on quartz glass substrates. The incorporation of P2 results in enhanced light absorption that is attributed to the increased light-harvesting capability of the perovskite films with larger grain size.

Hysteresis is a notorious phenomenon that degrades the overall device performance and operational stability, particularly for planar PSCs. Fig. 3a shows the typical *J–V* curves of the devices measured in both reverse and forward scan directions, with important device parameters listed in Table 3. It is observed that *J–V* hysteresis was substantially reduced by the addition of P2, while the pristine device showed pronounced hysteresis. For optimized PSCs, the *J–V* curves for reverse and forward scans almost overlap. The PCE measured under the reverse scan is 20.41%, while the PCE remains at 19.99% when measured under the forward scan. We believe that the significantly reduced hysteresis is attributed to the reduced defect density and efficient carrier transport from within the perovskite absorber layer achieved by P2 incorporation. The hysteresis index of the devices can be defined as[57]

$$\text{Hysteresis index} = \frac{\text{PCE}_{\text{reverse}} - \text{PCE}_{\text{forward}}}{\text{PCE}_{\text{reverse}}} \quad (1)$$

The hysteresis index for the optimized device is 0.020, which is noticeably lower than the value (0.133) for the pristine device.

To ensure the validity of the *J–V* measurements, a steady-state photocurrent output was measured, as presented in Fig. 3b. Steady-state photocurrent densities of 22.92 and 21.58 mA cm^{-2} were achieved at 0.923 and 0.862 V for the P2-optimized and reference devices, yielding stabilized power conversion outputs of 20.01% and 17.53%, respectively. It is observed that the steady-state power output for the P2-

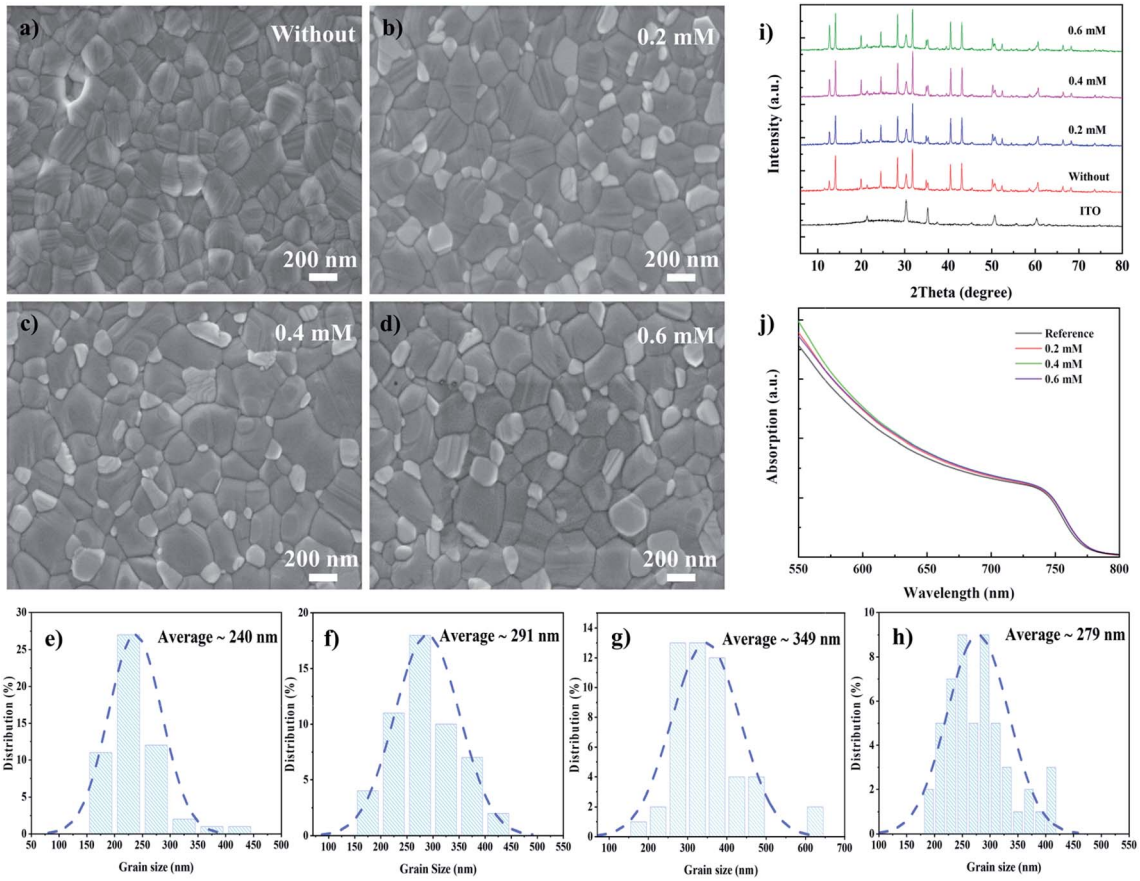

Fig. 2 (a–d) Surface topographic SEM images, and (e–h) grain size distributions of the $FA_{0.85}MA_{0.15}PbI_{2.55}Br_{0.45}$ films doped with different P2 concentrations. The crystal structure and optical properties of the perovskite films with different amounts of P2 (0, 0.2, 0.4, and 0.6 mM): (i) XRD patterns and (j) UV-vis absorption spectra.

optimized device maintained good stability, while the steady-state power output for the pristine device decayed slightly after 100 s. The steady-state photocurrent of the P2-optimized device was also recorded under simulated sunlight with 20 s light on/off cycles, as shown in Fig. S9.† An extremely fast and smooth photoresponse with stabilized performance characteristics was observed. These results demonstrate that the incorporation of P2 improves the operational stability of the PSC, most likely due to the more efficient charge carrier transport within and at the interfaces of the perovskite absorber layer. To demonstrate the reproducibility of this work, 50 individual devices were fabricated using the same procedure, with the statistical distributions of the key *J–V* parameters (J_{SC}, V_{OC}, FF, and PCE) presented in Fig. 3c–f. All of the key parameters exhibited relatively narrow distributions, indicating that the process was reproducible.

To investigate the origin of the improved device performance, the energy band positions of the perovskite films with and without P2 modification were analyzed by ultraviolet photoelectron spectroscopy (UPS). From the UPS results presented in Fig. 4a, the work functions (WFs) of the reference and P2-optimized perovskite films were determined by subtracting the cut-off energies of the secondary electrons from the He I excitation energy (21.22 eV). Therefore, the Fermi levels (E_F) lie 4.22 and 4.00 eV below the vacuum level (E_{VAC}) for the reference and P2-optimized perovskite films, respectively. From the valence band spectra in Fig. 4b, the valence band positions of the reference and P2-optimized perovskite films were found to be 1.41 and 1.49 eV below their Fermi levels, respectively. Combined with the band gaps obtained from the Tauc plots of the absorption spectra (Fig. S10†), the detailed energy levels of the reference and P2-optimized perovskite films are shown in Fig. 4c. According to the band positions of the NiO_x HTL and Nb_2O_5 ETL obtained in our previous study,[25] the schematic energy diagrams of the reference and optimized devices are shown in Fig. 4d. These results reveal that P2 modification shifts the conduction band edge (CBE) and valence band edge (VBE) upward, resulting in better alignment of the CBE and VBE energies with those of the NiO_x HTL and Nb_2O_5 ETL. In particular, the CB of the P2-optimized perovskite becomes higher than that of the Nb_2O_5 ETL, eliminating the barrier for electron extraction. This most likely accounts for the increased V_{OC} of the P2-optimized device. Moreover, the E_F of the P2-optimized perovskite comes closer to the CB, suggesting an improved conductivity of the perovskite film that can contribute to the improved FF of the P2-optimized device.

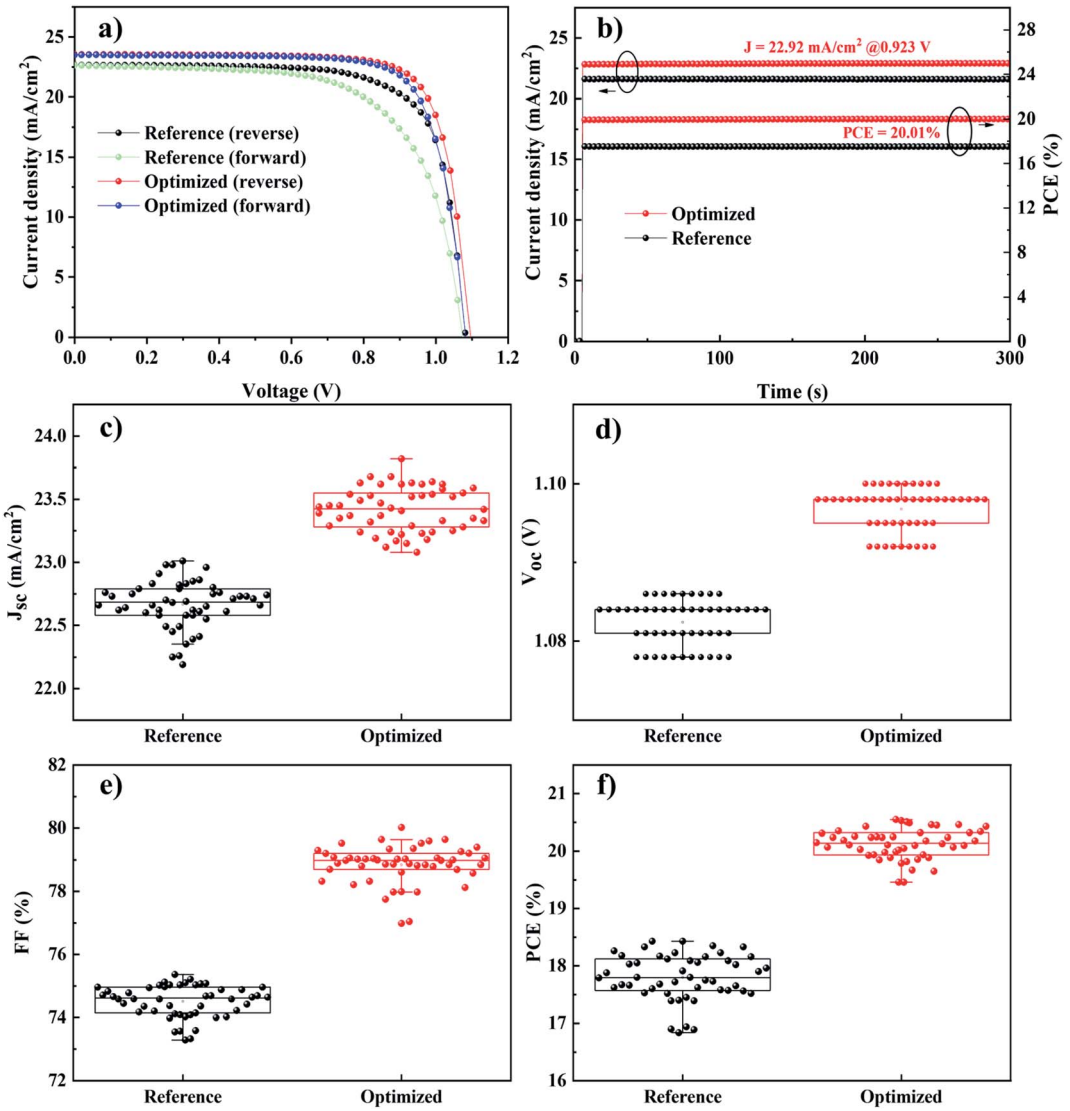

Fig. 3 (a) J–V characteristics in reverse and forward scan directions. (b) Steady-state photocurrent and power conversion output of the corresponding PSCs. Statistical distributions of the J–V parameters for 50 P2-optimized and reference devices: (c) J_{SC}, (d) V_{OC}, (e) FF, and (f) PCE.

Steady-state and time-resolved photoluminescence (TRPL) was carried out to investigate the effect of P2 incorporation on the charge transfer and recombination kinetics of the perovskite films. Comparison of the perovskite films deposited on a quartz glass substrate shows that the PL intensity was enhanced by over 30% upon P2 incorporation (Fig. 5a). Meanwhile, with P2 incorporation the peak position blue-shifted from 772 to 765 nm and the full-width-at-half-maximum (FWHM) of the spectra decreased from 47.0 to 44.4 nm. These results indicate that P2 incorporation may passivate defects in the perovskite film. For the perovskite films deposited on the NiO_x-coated ITO substrates, the PL intensity was quenched to a greater extent in the P2-optimized sample, suggesting more effective hole extraction at the interface between the NiO_x and the P2-optimized perovskite film. In agreement with the PL data, the TRPL results in Fig. 5b show that with P2

Table 3 The key J–V parameters and hysteresis index of the reference and P2-optimized PSCs

Device	Scanning mode	V_{OC} (V)	J_{SC} (mA cm^{-2})	FF (%)	PCE (%)	Hysteresis index
Optimized	Reverse	1.098	23.59	78.8	20.41	0.020
	Forward	1.086	23.51	78.3	19.99	
Reference	Reverse	1.083	22.66	74.5	18.28	0.133
	Forward	1.074	22.63	65.2	15.84	

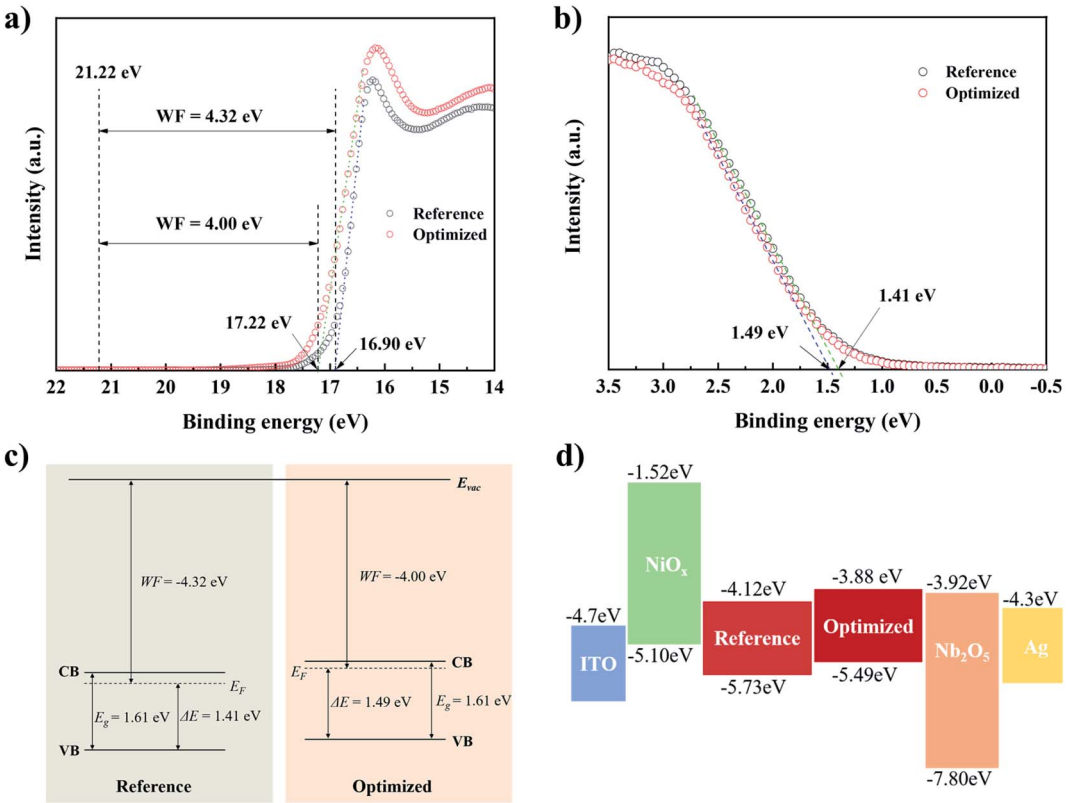

Fig. 4 UPS spectra of perovskite films without and with the addition of 0.4 mM P2 (a) near the cutoff energy, and (b) near the valence band edge. (c) Comparison of energy levels of perovskite films. (d) Schematic energy diagram.

incorporation the average lifetime increased from 1.489 to 1.815 μs for the samples deposited on quartz glass substrates, while it decreased from 0.344 to 0.212 μs for the samples deposited on the NiO_x-coated ITO substrates (Table S1†). These results demonstrate that P2 incorporation reduces the trap density and improves charge transfer within the bulk and at the NiO_x/perovskite interface *via* effective coordination between the carboxylate moieties and the undercoordinated Pb^{2+} at the grain boundaries and on the surfaces, leading to improved photovoltaic performance in the P2-optimized PSCs.

To further elucidate the role of P2 in the improved PSC performance, the recombination and transport resistances were investigated by electronic impedance spectroscopy (EIS),[58] as shown in Fig. 5c. The Nyquist plots for the pristine and P2-optimized devices were measured in the dark. The equivalent circuit model comprising the series resistance (R_s), the recombination resistance (R_{rec}) and capacitance (C_{rec}) is depicted in the inset of Fig. 5c. The fitted parameters for the Nyquist plots are summarized in Table S2.† The value of R_s decreased from 9.85 to 5.36 Ω after the P2 modification, indicating that P2 incorporation facilitates carrier transport. A more pronounced change from 150.2 Ω in the reference cell to 358.3 Ω in the optimized device was found for R_{rec}. The much larger R_{rec} in the optimized device indicates the effective suppression of charge recombination that may originate from the passivation of the traps by P2 modification. Meanwhile, the effective lifetimes (τ_n) were extracted from the complex plane curves as the reciprocals of the frequencies at the peaks of the semicircles in the Cole–Cole plots.[59] The τ_n of the optimized device (6.34 μs) is considerably longer than that of the reference cell (3.99 μs), indicating that photogenerated carriers were transported for a longer time to the electrodes prior to possible recombination. Therefore, the above results confirm that P2 incorporation effectively passivates the trap states in the perovskite films and promotes the transport of charge carriers, resulting in improved photovoltaic performance.

The space charge limited current (SCLC) method was employed to determine the trap density in the perovskite films. Fig. 5d shows the *I–V* curves of the electron-only perovskite devices with the ITO/Nb_2O_5/perovskite/Nb_2O_5/Ag architecture. The current increases linearly in the low-bias-voltage region and a non-linear sharp increase is observed when the bias voltage exceeds the kink point that is defined as the trap-filled limit voltage (V_{TFL}). The trap-state density (n_t) can be calculated according to the following equation[60]

$$n_t = \frac{2\varepsilon\varepsilon_0 V_{TFL}}{eL^2} \quad (2)$$

where e is the elementary charge, L is the thickness of the film, and ε_0 and ε are the vacuum permittivity and relative dielectric constant of perovskite ($\varepsilon = 28.8$), respectively. The V_{TFL} values of the pristine and P2-optimized perovskite films were measured to be 0.601 and 0.224 V, respectively. The corresponding trap-state densities for the pristine and P2-optimized perovskite

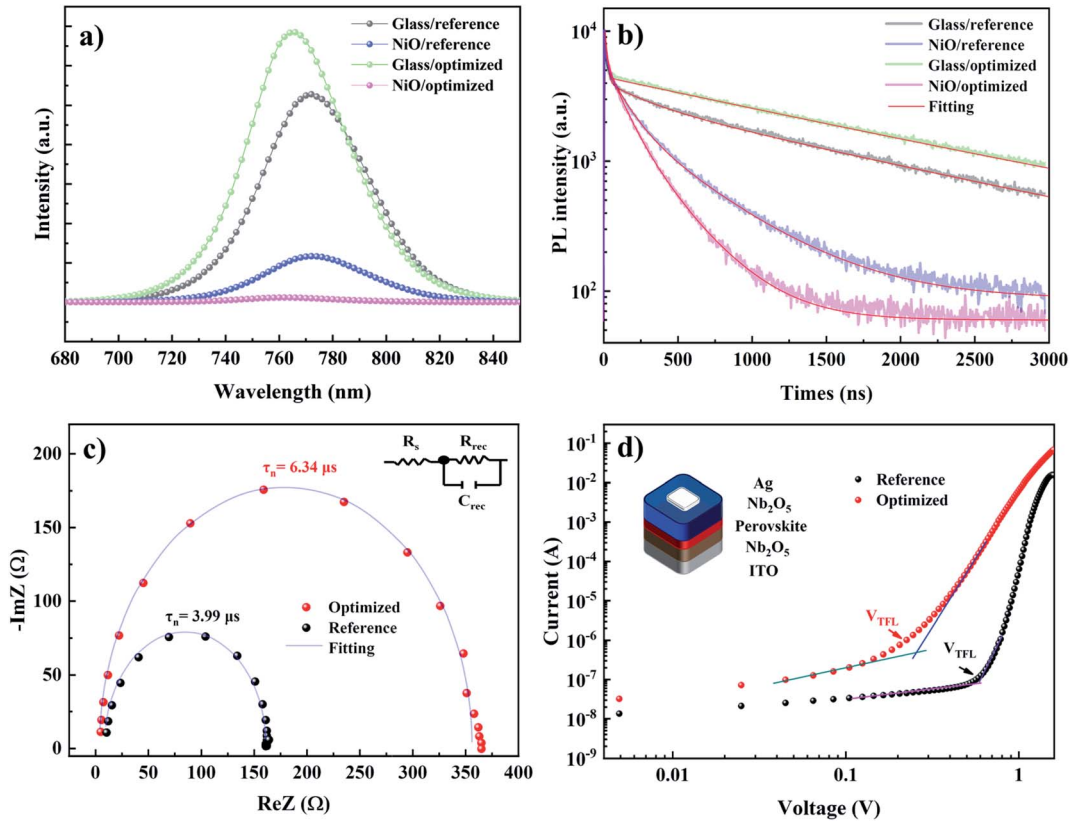

Fig. 5 (a) Steady-state PL spectra and (b) TRPL decay curves of the reference and P2-optimized perovskite films deposited on different substrates. (c) Nyquist plots of the reference and P2-optimized PSCs. (d) Dark *I*–*V* plots of the electron-only perovskite device depicted in the inset.

films were calculated to be 5.32×10^{15} cm^{-3} and 1.98×10^{15} cm^{-3}, respectively, clearly demonstrating the reduction of the trap-state density by a factor of ~2.7.

The improvement of the moisture endurance of the perovskite film by the incorporation of the P2 polymer may be due to the following mechanisms depicted in Fig. 6a. First, the high hydrophobicity of the fluoride ion within P2 effectively prevents the external moisture ingress into the perovskite films. Furthermore, the C=O group of P2 can form hydrogen bonds with the cation in the perovskite, and the formation of such hydrogen bonds balances the electron cloud density of the organic cation, hindering the octahedral tilting of the corner-sharing $[PbI_6]^{4-}$ black phase through the reduction of the stretching vibration frequency. This will improve the intrinsic stability of the perovskite film. Even with moisture infiltration at high humidity, P2 in the perovskite can absorb some of the water molecules to form carboxylic acid groups through the hydrolysis of the side-chain ester groups, which can also passivate the surface electronic trap states *via* efficient coordination between the carboxylate moieties.[61] The passivation decreases the chemical activity of the perovskite surface to suppress the hydration reaction.

To provide physical evidence for the above mechanism, the contact angle of the water droplet on the perovskite films was measured with the results shown in Fig. 6b. The pristine perovskite film showed a small contact angle of 57°, while the P2-modified films presented larger contact angles of 63°, 67°, and 74° for various P2 concentrations. It is clear that the contact angle increased with increasing P2 concentrations, demonstrating that the addition of P2 can effectively prevent water molecules from entering the perovskite film. Therefore, the P2 incorporation into the perovskite layer acts as an effective barrier against humidity, enhancing the overall device stability. To probe the interaction between P2 and the perovskite, we measured the ^{1}H NMR (Fig. S11†) and Fourier transform infrared (FTIR) spectra (Fig. S12†) of the perovskite precursor solution in the absence and presence of P2 in deuterated dimethyl sulfoxide-d6 (DMSO-d6). The NMR spectra in Fig. 6c show a single broad peak at δ = 8.585 ppm for the pristine perovskite sample that is ascribed to the FA amine hydrogen (NH and NH_2).[62] In contrast, peak splitting of the ^{1}H NMR peak was observed in the precursor solution with the addition of P2 and these peaks showed a downfield shift. This is most likely due to the C=N double bond vibration in the FA^+ cation that causes the FA amine hydrogen atoms (NH and NH_2) to be in similar chemical environments so that only one broad peak at 8.585 ppm is observed. However, the P2 addition leads to the splitting of the NMR peak of the amine hydrogen and imine hydrogen in FA. This indicates that the carbonyl group (C=O) in P2 forms a hydrogen bond with the amine hydrogen (NH) in FA,

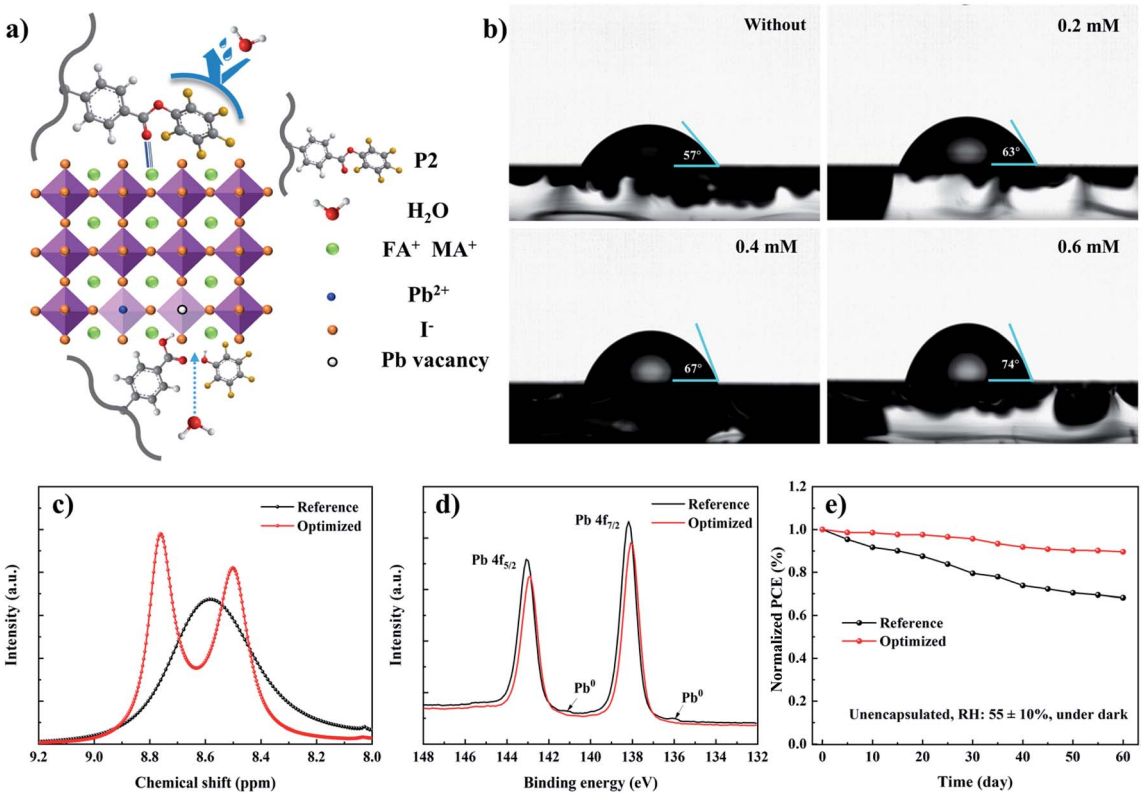

Fig. 6 (a) Proposed mechanism for the enhanced stability of P2-modified perovskite films. (b) Static contact angle measurements with water droplets on top of the perovskite films with different P2 concentrations. (c) ^{1}H NMR spectra of the perovskite precursor solution with and without P2. (d) Core-level XPS spectra of Pb 4f for perovskite films with and without P2. (e) Stability tests for PSCs stored in air with 55 ± 10% RH for 60 days at room temperature.

significantly reducing the vibration of the FA double bond and changing the environment of the FA amine hydrogen atoms (NH and NH_2). This change leads to the observed peak splitting. The FTIR spectra presented in Fig. S12† show that the C=N stretching vibration peak slightly shifted to a lower wavenumber in the P2-doped perovskite film, indicating a change of the C=N double bond vibration likely due to the formation of a hydrogen bond. X-ray photoelectron spectroscopy (XPS) wide-scan results of the perovskite films did not show any significant change following the P2 doping (Fig. S13†). No F signal was detected in the P2-doped perovskite, most likely because its concentration is below the detection limit. Nevertheless, the core-level XPS spectra of Pb 4f in Fig. 6d reveal that the presence of metallic Pb on the surface of the perovskite is suppressed by P2 doping. The appearance of metallic Pb in the pristine perovskite film may be due to the existence of iodine and cation vacancies that have been recognized as the most important non-radiative recombination centers.[63] In contrast, there were no detectable signals for metallic Pb in the P2-modified perovskite, indicating that the undercoordinated Pb atoms have been effectively reduced after P2 doping. Meanwhile, the peak position of the Pb 4f shifted noticeably, indicating the formation of new chemical coordination bonds on the perovskite surface. Therefore, the reaction between ambient water molecules and the perovskite films may be inhibited and the formed organic terminal groups can passivate the iodine and cation vacancies, resulting in the remarkably improved device performance and stability.

Based on the above discussion, it is concluded that the P2-modified perovskite films can not only improve the passivation and stability but also strongly inhibit the reaction between the ambient water molecules and perovskite films. Therefore, we studied the moisture stability of the perovskite films and PSC devices with and without P2 doping. The perovskite films and PSC devices without any encapsulation were tested upon exposure to the ambient environment (in air at a relative humidity of 55 ± 10% at 25 °C). The color of the pristine perovskite film changed from dark brown to yellowish after 30 days, indicating the decomposition of the perovskite into PbI_2, as evidenced by the intense PbI_2 peak at 12.68° in the XRD pattern of the sample (Fig. S14a†). In contrast, the color of the P2-modified perovskite film remained almost unchanged and the intensity of the PbI_2 diffraction peak increased only slightly within the same period (Fig. S14b†), indicating a significant improvement of moisture stability. Consequently, the P2-optimized device retained 90% of its initial PCE value after storage in air for 60 days, as shown in Fig. 6e. In contrast, the PCE of the pristine device decreased to 68% of its initial value after the same aging. The stability tests demonstrated that the P2-optimized devices have the potential for showing stability in harsh environments.

Conclusions

In summary, we propose a novel strategy for the synthesis of stable and highly efficient inverted perovskite solar cells with all-inorganic charge extraction layers exceeding 20% PCE through the incorporation of a polyacetylene derivative into the perovskite active layer. The interaction of the P2 polymer with the perovskite precursor not only effectively passivates the defects in the perovskite but also improves the charge extraction efficiency and the water resistance of the perovskite films. As a result, the P2-optimized device exhibits the highest PCE of 20.41% reported to date for inverted PSCs based on all-inorganic charge extraction layers. More importantly, the device shows excellent long-term stability, retaining 90% of its initial PCE after exposure for 60 days to air with a relative humility of 55 ± 10%. This work offers an approach for developing high-performance PSCs and provides another potential route toward PSC commercialization.

Experimental section

Materials preparation

All the chemicals were used as received without further purification. Lead iodide (PbI_2, 99.9985%) was purchased from Alfa Aesar; lead bromide ($PbBr_2$, 99.999%) was purchased from Aladdin. Dehydrated solvents of chlorobenzene (CB, 99.9%), dimethyl sulfoxide (DMSO, 99.9%) and *N*,*N*-dimethylformamide (DMF, 99.9%) were purchased from Sigma-Aldrich. Silver (Ag, 99.999%), nickel oxide (NiO, 99.9%), and niobium oxide (Nb_2O_5, 99.9%) were purchased from ZhongNuo Advanced Material (Beijing) Technology. The chemicals and detailed procedures for the synthesis of the polyacetylene derivative polymers are given in the ESI.†

Perovskite solution preparation. $FA_{0.85}MA_{0.15}PbI_{2.55}Br_{0.45}$ solution (1.2 M) was prepared in a mixed solvent of DMF and DMSO with a volume ratio of 4 : 1. The molar ratios for PbI_2/$PbBr_2$ and FAI/MABr were both fixed at 0.85 : 0.15, and the molar ratio of (FAI + MABr)/(PbI_2 + $PbBr_2$) was fixed at 1 : 1. Prepared solutions were filtered through a 0.22 μm pore PTFE syringe filter after stirring at 60 °C for 24 h and were stored in a dry nitrogen atmosphere. For polyacetylene derivative doping, the polymers were directly added to the perovskite precursor solution at desired concentrations.

Perovskite solar cell fabrication

Preparation of the NiO_x hole transport layer. Pre-patterned ITO/glass substrates (Yaoke Optoelectronics, 10 Ω sq^{-1}) with sizes of 1.4 × 1.6 cm^2 were ultrasonically cleaned with a 1% Alconox detergent diluted in deionized water, deionized water, acetone, and isopropanol (IPA) in succession each for 15 min, and dried under a nitrogen stream. Then, a 30 nm thick NiO_x film was deposited onto the ITO substrates by electron beam (EB) evaporation (Angstrom Engineering, AMOD) at a base pressure of $<5 \times 10^{-6}$ Torr and a deposition rate of ~1 Å s^{-1}. Post-annealing of the NiO_x thin films was carried out in a tube furnace in air at 300 °C for 1 h.

Deposition of perovskite films. Perovskite films were deposited using a simple one-step spin-coating method. The NiO_x-coated ITO substrates were transferred into an N_2-filled glovebox and the $FA_{0.85}MA_{0.15}PbI_{2.55}Br_{0.45}$ precursor solutions with or without the polyacetylene derivative polymers were spin-cast onto the substrate at a speed of 4000 rpm for 40 s and CB (100 μL) was dropped onto the spinning substrate during the spin-coating step 20 s before the end of the procedure. Then, the films were heated on a hotplate at 150 °C for 15 min.

Final PSC device assembly. Nb_2O_5 thin film with a thickness of 60 nm was deposited onto the perovskite layer by EB evaporation at a deposition rate of approximately 1 Å s^{-1}. Finally, a Ag electrode (99.99%, 100 nm) was deposited on top of the Nb_2O_5 ETL through a metal shadow mask by EB evaporation at a base pressure of ~5×10^{-6} Torr and a deposition rate of approximately 2 Å s^{-1} as the back contact. The active area of the solar cells was 0.160 cm^2 and the unencapsulated devices were stored under dry conditions and characterized under an ambient atmosphere.

Materials characterization

The surface morphology was characterized using a scanning electron microscope (SEM, ZEISS Crossbeam 340). X-ray diffraction (XRD; Thermo Scientific ARL EQUINOX 1000) was measured using a Cu Kα radiation source operated at 40 kV and 30 mA. The absorption spectra of the samples were measured by UV-visible spectroscopy (UV-Vis; UV-1900, SHIMADZU) and calculated *via* Tauc analysis according to the equation $(\alpha h\nu)^2 = A(h\nu - E_g)$. The photocurrent density–voltage (*J*–*V*) curves were measured under the reverse scan (open-circuit bias to short-circuit bias) using an AAA class solar simulator (SAN-EI ELECTRIC, XES-40S2) as the light source at 25 °C. Before the use of the light source, the light intensity was calibrated to 1 sun (100 mW cm^{-2}) using a certified reference cell (Konica Minolta AK-200). The spectral response was obtained using an EQE measurement system (QEX10, PV Measurements), which is equipped with a monochromator, a lock-in amplifier, a Xe lamp, and a current–voltage amplifier. The frequency-dependent capacitance (C-f) of the device was measured using a potentiostat (Bio-Logic SP-200). The AC voltage perturbation was 20 mV, and a constant zero bias was maintained. Each spectrum was measured at frequencies ranging from 1 kHz to 1 MHz. Regarding nuclear magnetic resonance (NMR) spectroscopy, ^{1}H NMR spectra were recorded on a JNM-ECZ400S/L1 400 MHz NMR spectrometer. Deuterated dimethyl sulfoxide (DMSO-d6) and deuterated chloroform ($CDCl_3$) were used as solvents. XPS measurements were performed using a Kratos-Axis Supra system with a monochromatized Al Kα X-ray source under a pressure of 5.0 × 10^{-7} Pa. UPS measurements were carried out with a Thermo Fisher Scientific ESCALAB 250 Xi using the He I line (21.22 eV) as the excitation source.

Author contributions

JJ and XL contributed equally to this work. JJ, XL, HZ, and YL conceived the idea and designed the experiments. JJ and XL

performed the experiments and analyzed the data. JJ, MBF, and YL wrote the manuscript. All authors reviewed and commented on the manuscript.

Conflicts of interest

The authors declare no competing financial interests.

Acknowledgements

This work was supported by the National Natural Science Foundation of China (No. 21872019) and Sichuan Science and Technology Foundation (No. 2018JY0137).

References

1 H. Zhou, Q. Chen, G. Li, S. Luo, T.-b. Song, H.-S. Duan, Z. Hong, J. You, Y. Liu and Y. Yang, *Science*, 2014, **345**, 542–546.
2 Q. Wang, N. Phung, D. Di Girolamo, P. Vivo and A. Abate, *Energy Environ. Sci.*, 2019, **12**, 865–886.
3 J. Chen and N. G. Park, *Adv. Mater.*, 2019, **31**, 1803019.
4 C. Liu, J. Yuan, R. Masse, X. Jia, W. Bi, Z. Neale, T. Shen, M. Xu, M. Tian, J. Zheng, J. Tian and G. Cao, *Adv. Mater.*, 2020, **32**, 1905245.
5 S. S. Shin, E. J. Yeom, W. S. Yang, S. Hur, M. G. Kim, J. Im, J. Seo, J. H. Noh and S. I. Seok, *Science*, 2017, **356**, 167–171.
6 M. Zhang, M. Ye, W. Wang, C. Ma, S. Wang, Q. Liu, T. Lian, J. Huang and Z. Lin, *Adv. Mater.*, 2020, **32**, 2000999.
7 T. Abzieher, S. Moghadamzadeh, F. Schackmar, H. Eggers, F. Sutterlüti, A. Farooq, D. Kojda, K. Habicht, R. Schmager, A. Mertens, R. Azmi, L. Klohr, J. A. Schwenzer, M. Hetterich, U. Lemmer, B. S. Richards, M. Powalla and U. W. Paetzold, *Adv. Energy Mater.*, 2019, **9**, 1802995.
8 C. M. Wolff, P. Caprioglio, M. Stolterfoht and D. Neher, *Adv. Mater.*, 2019, **31**, 1902762.
9 M. Saliba, T. Matsui, K. Domanski, J. Y. Seo, A. Ummadisingu, S. M. Zakeeruddin, J. P. Correa-Baena, W. R. Tress, A. Abate, A. Hagfeldt and M. Gratzel, *Science*, 2016, **354**, 206–209.
10 A. Kojima, K. Teshima, Y. Shirai and T. Miyasaka, *J. Am. Chem. Soc.*, 2009, **131**, 6050–6051.
11 X. Hu, C. Liu, Z. Zhang, X. F. Jiang, J. Garcia, C. Sheehan, L. Shui, S. Priya, G. Zhou, S. Zhang and K. Wang, *Adv. Sci.*, 2020, **7**, 2001285.
12 D. Yang, X. Zhang, K. Wang, C. Wu, R. Yang, Y. Hou, Y. Jiang, S. Liu and S. Priya, *Nano Lett.*, 2019, **19**, 3313–3320.
13 J. Jiang, Z. Jin, J. Lei, Q. Wang, X. Zhang, J. Zhang, F. Gao and S. Liu, *J. Mater. Chem. A*, 2017, **5**, 9514–9522.
14 N. J. Jeon, J. H. Noh, W. S. Yang, Y. C. Kim, S. Ryu, J. Seo and S. I. Seok, *Nature*, 2015, **517**, 476–480.
15 S. Rong, Y. Xiao, J. Jiang, Q. Zeng and Y. Li, *J. Phys. Chem. C*, 2020, **124**, 8992–8998.
16 H. Kanda, N. Shibayama, A. J. Huckaba, Y. Lee, S. Paek, N. Klipfel, C. Roldán-Carmona, V. I. E. Queloz, G. Grancini, Y. Zhang, M. Abuhelaiqa, K. T. Cho, M. Li, M. D. Mensi, S. Kinge and M. K. Nazeeruddin, *Energy Environ. Sci.*, 2020, **13**, 1222–1230.
17 H. Ren, S. Yu, L. Chao, Y. Xia, Y. Sun, S. Zuo, F. Li, T. Niu, Y. Yang, H. Ju, B. Li, H. Du, X. Gao, J. Zhang, J. Wang, L. Zhang, Y. Chen and W. Huang, *Nat. Photonics*, 2020, **14**, 154–163.
18 N. K. Noel, S. N. Habisreutinger, A. Pellaroque, F. Pulvirenti, B. Wenger, F. Zhang, Y.-H. Lin, O. G. Reid, J. Leisen, Y. Zhang, S. Barlow, S. R. Marder, A. Kahn, H. J. Snaith, C. B. Arnold and B. P. Rand, *Energy Environ. Sci.*, 2019, **12**, 3063–3073.
19 E. Shi, B. Yuan, S. B. Shiring, Y. Gao, Akriti, Y. Guo, C. Su, M. Lai, P. Yang, J. Kong, B. M. Savoie, Y. Yu and L. Dou, *Nature*, 2020, **580**, 614–620.
20 D. Bogachuk, S. Zouhair, K. Wojciechowski, B. Yang, V. Babu, L. Wagner, B. Xu, J. Lim, S. Mastroianni, H. Pettersson, A. Hagfeldt and A. Hinsch, *Energy Environ. Sci.*, 2020, **13**, 3880–3916.
21 M. Azam, S. Yue, R. Xu, K. Liu, K. Ren, Y. Sun, J. Liu, Z. Wang, S. Qu, Y. lei and Z. Wang, *J. Mater. Chem. A*, 2018, **6**, 13725–13734.
22 P. Wang, X. Zhang, Y. Zhou, Q. Jiang, Q. Ye, Z. Chu, X. Li, X. Yang, Z. Yin and J. You, *Nat. Commun.*, 2018, **9**, 2225.
23 K. Rakstys, C. Igci and M. K. Nazeeruddin, *Chem. Sci.*, 2019, **10**, 6748–6769.
24 J. You, L. Meng, T. B. Song, T. F. Guo, Y. M. Yang, W. H. Chang, Z. Hong, H. Chen, H. Zhou, Q. Chen, Y. Liu, N. De Marco and Y. Yang, *Nat. Nanotechnol.*, 2016, **11**, 75–81.
25 X. Liu, J. Jiang, F. Wang, Y. Xiao, I. D. Sharp and Y. Li, *ACS Appl. Mater. Interfaces*, 2019, **11**, 46894–46901.
26 X. Liu, Y. Xiao, Q. Zeng, J. Jiang and Y. Li, *J. Phys. Chem. Lett.*, 2019, **10**, 6382–6388.
27 S. Yue, K. Liu, R. Xu, M. Li, M. Azam, K. Ren, J. Liu, Y. Sun, Z. Wang, D. Cao, X. Yan, S. Qu, Y. Lei and Z. Wang, *Energy Environ. Sci.*, 2017, **10**, 2570–2578.
28 Y. Li, J. K. Cooper, R. Buonsanti, C. Giannini, Y. Liu, F. M. Toma and I. D. Sharp, *J. Phys. Chem. Lett.*, 2015, **6**, 493–499.
29 Z. Wu, M. Jiang, Z. Liu, A. Jamshaid, L. K. Ono and Y. Qi, *Adv. Energy Mater.*, 2020, **10**, 1903696.
30 Y. Lv, R. Yuan, B. Cai, B. Bahrami, A. H. Chowdhury, C. Yang, Y. Wu, Q. Qiao, S. F. Liu and W. H. Zhang, *Angew. Chem., Int. Ed.*, 2020, **59**, 11969–11976.
31 B. Zhang, J. Su, X. Guo, L. Zhou, Z. Lin, L. Feng, J. Zhang, J. Chang and Y. Hao, *Adv. Sci.*, 2020, **7**, 1903044.
32 M. B. Faheem, B. Khan, C. Feng, M. U. Farooq, F. Raziq, Y. Xiao and Y. Li, *ACS Energy Lett.*, 2019, **5**, 290–320.
33 Y. Li, J. K. Cooper, W. Liu, C. M. Sutter-Fella, M. Amani, J. W. Beeman, A. Javey, J. W. Ager, Y. Liu, F. M. Toma and I. D. Sharp, *Nat. Commun.*, 2016, **7**, 12446.
34 Q. Zhou, L. Liang, J. Hu, B. Cao, L. Yang, T. Wu, X. Li, B. Zhang and P. Gao, *Adv. Energy Mater.*, 2019, **9**, 1802595.
35 M. Zhang, Q. Chen, R. Xue, Y. Zhan, C. Wang, J. Lai, J. Yang, H. Lin, J. Yao, Y. Li, L. Chen and Y. Li, *Nat. Commun.*, 2019, **10**, 4593.

36 Y. Zhang, S. Seo, S. Y. Lim, Y. Kim, S.-G. Kim, D.-K. Lee, S.-H. Lee, H. Shin, H. Cheong and N.-G. Park, *ACS Energy Lett.*, 2019, **5**, 360–366.
37 Y. Cao, Y. Li, T. Morrissey, B. Lam, B. O. Patrick, D. J. Dvorak, Z. Xia, T. L. Kelly and C. P. Berlinguette, *Energy Environ. Sci.*, 2019, **12**, 3502–3507.
38 Y. Dong, J. Zhang, Y. Yang, L. Qiu, D. Xia, K. Lin, J. Wang, X. Fan and R. Fan, *Angew. Chem., Int. Ed.*, 2019, **58**, 17610–17615.
39 Y. Zhou, X. Yin, Q. Zhang, N. Wang, A. Yamamoto, K. Koumoto, H. Shen and H. Lin, *Mater. Today Energy*, 2019, **12**, 363–370.
40 P. Cui, D. Wei, J. Ji, H. Huang, E. Jia, S. Dou, T. Wang, W. Wang and M. Li, *Nat. Energy*, 2019, **4**, 150–189.
41 H. Tan, F. Che, M. Wei, Y. Zhao, M. I. Saidaminov, P. Todorovic, D. Broberg, G. Walters, F. Tan, T. Zhuang, B. Sun, Z. Liang, H. Yuan, E. Fron, J. Kim, Z. Yang, O. Voznyy, M. Asta and E. H. Sargent, *Nat. Commun.*, 2018, **9**, 3100.
42 Y. Li, K. R. Scheel, R. G. Clevenger, W. Shou, H. Pan, K. V. Kilway and Z. Peng, *Adv. Energy Mater.*, 2018, **8**, 1801248.
43 Y. Chen, Z. Yang, S. Wang, X. Zheng, Y. Wu, N. Yuan, W. H. Zhang and S. F. Liu, *Adv. Mater.*, 2018, **30**, 1805660.
44 H. Zhang, Y. Wu, C. Shen, E. Li, C. Yan, W. Zhang, H. Tian, L. Han and W. H. Zhu, *Adv. Energy Mater.*, 2019, **9**, 1803573.
45 H. Chen, T. Liu, P. Zhou, S. Li, J. Ren, H. He, J. Wang, N. Wang and S. Guo, *Adv. Mater.*, 2020, **32**, 1905661.
46 Q. Xiao, J. Tian, Q. Xue, J. Wang, B. Xiong, M. Han, Z. Li, Z. Zhu, H. L. Yip and Z. Li, *Angew. Chem., Int. Ed.*, 2019, **58**, 17724–17730.
47 H. Li, J. Shi, J. Deng, Z. Chen, Y. Li, W. Zhao, J. Wu, H. Wu, Y. Luo, D. Li and Q. Meng, *Adv. Mater.*, 2020, **32**, 1907396.
48 J. Jiang, Q. Wang, Z. Jin, X. Zhang, J. Lei, H. Bin, Z.-G. Zhang, Y. Li and S. F. Liu, *Adv. Energy Mater.*, 2018, **8**, 1701757.
49 T. Wu, Y. Wang, Z. Dai, D. Cui, T. Wang, X. Meng, E. Bi, X. Yang and L. Han, *Adv. Mater.*, 2019, **31**, 1900605.
50 T. Wu, Y. Wang, X. Li, Y. Wu, X. Meng, D. Cui, X. Yang and L. Han, *Adv. Energy Mater.*, 2019, **9**, 1803766.
51 Y. Zhao, J. Wei, H. Li, Y. Yan, W. Zhou, D. Yu and Q. Zhao, *Nat. Commun.*, 2016, **7**, 10228.
52 L. Liu, Y. Kan, K. Gao, J. Wang, M. Zhao, H. Chen, C. Zhao, T. Jiu, A. K. Jen and Y. Li, *Adv. Mater.*, 2020, **32**, 1907604.
53 P. Holzhey and M. Saliba, *J. Mater. Chem. A*, 2018, **6**, 21794–21808.
54 W. Hui, Y. Yang, Q. Xu, H. Gu, S. Feng, Z. Su, M. Zhang, J. Wang, X. Li, J. Fang, F. Xia, Y. Xia, Y. Chen, X. Gao and W. Huang, *Adv. Mater.*, 2020, **32**, 1906374.
55 G. M. Kim, A. Ishii, S. Öz and T. Miyasaka, *Adv. Energy Mater.*, 2020, **10**, 1903299.
56 H. Wang, Z. Wang, Z. Yang, Y. Xu, Y. Ding, L. Tan, C. Yi, Z. Zhang, K. Meng, G. Chen, Y. Zhao, Y. Luo, X. Zhang, A. Hagfeldt and J. Luo, *Adv. Mater.*, 2020, **32**, 2000865.
57 J. Jiang, Z. Jin, F. Gao, J. Sun, Q. Wang and S. F. Liu, *Adv. Sci.*, 2018, **5**, 1800474.
58 B. J. Leever, C. A. Bailey, T. J. Marks, M. C. Hersam and M. F. Durstock, *Adv. Energy Mater.*, 2012, **2**, 120–128.
59 Z. Jin, M. Yuan, H. Li, H. Yang, Q. Zhou, H. Liu, X. Lan, M. Liu, J. Wang, E. H. Sargent and Y. Li, *Adv. Funct. Mater.*, 2016, **26**, 5284–5289.
60 D. Bai, H. Bian, Z. Jin, H. Wang, L. Meng, Q. Wang and S. Liu, *Nano Energy*, 2018, **52**, 408–415.
61 S. Wang, H. Chen, J. Zhang, G. Xu, W. Chen, R. Xue, M. Zhang, Y. Li and Y. Li, *Adv. Mater.*, 2019, **31**, 1903691.
62 A. Solanki, M. M. Tavakoli, Q. Xu, S. S. H. Dintakurti, S. S. Lim, A. Bagui, J. V. Hanna, J. Kong and T. C. Sum, *Adv. Mater.*, 2020, **32**, 1907864.
63 H. Kanda, N. Shibayama, M. Abuhelaiqa, S. Paek, R. Kaneko, N. Klipfel, A. A. Sutanto, C. R. Carmona, A. J. Huckaba, H. Kim, C. Momblona, A. M. Asiri and M. K. Nazeeruddin, *J. Mater. Chem. A*, 2020, **8**, 17113–17119.

